Chapter 2: Determination of Melt Influence on Divalent Element Partitioning between Anorthite and CMAS melts[*]

2.1 INTRODUCTION

Trace element distributions between mineral and melt phases have proven to be important tools in understanding differentiation histories of lunar and terrestrial rocks. One important basis for their value is the apparent simplicity in trace element behavior that arises from Henry's Law – at low concentrations, the partition coefficient D_i, defined after Nernst as [concentration of element i in crystal phase]/[concentration of element i in melt phase] (Beattie et al., 1993), is found to be independent of the concentration of the trace element. Most modeling of igneous processes continues to employ a constant partition coefficient to describe distribution of a particular element between melts and each mineral phase of interest. In reality, however, mineral/melt partition coefficients vary with pressure, temperature, and the major-element compositions of the melt and mineral phases. Ideally, therefore, differentiation models should be able to dynamically account for changing partitioning behavior over the course of magma evolution.

The chemical complexity of natural systems prevents experimental determination of equilibrium trace element partitioning in systems containing all possible combinations of components and physical conditions (i.e., temperature, pressure, oxygen fugacity) of interest. Even a set of high-quality experimental data customized to the situation of

interest requires an interpolation scheme for use in numerical models. In the interest of overcoming such limitations, development of predictive models for trace element partitioning continues to be an area of active research. Blundy and Wood (1994) and Wood and Blundy (2001) describe a quite successful formalism that represents considerable progress towards a general predictive model of trace element partitioning. In particular, it explains the observed parabolic relationship between the cation radius and the logarithm of the partition coefficients of various homovalent trace elements for a given crystal (Higuchi and Nagasawa, 1969; Onuma et al., 1968). The model incorporates the Brice (1975) model of crystal lattice strain energy, taken to be a function of misfit in radius between a substituting cation and a particular crystallographic site, into a general expression for partitioning:

$$D_i(P,T,X) = D_o(P,T,X) \exp\left[-4\pi E N_A \left[\frac{r_o}{2}(r_i - r_o)^2 + \frac{1}{3}(r_i - r_o)^3 \right] / RT \right], \quad (2.1)$$

where r_i is the ionic radius of cation i; r_o, the ideal (strain-free) radius of the lattice site; D_o, the partition coefficient of an ideally sized cation for that lattice site; and E, a strain parameter for the site. N_A is Avogadro's number, R is the gas constant, and T is absolute temperature. Extensions of this model have investigated prediction of the r_o and E parameters from macroscopic structural and elastic data on the host phase (e.g.,Purton et al., 1996; Purton et al., 2000), systematics of variations in the fit parameters with mineral composition along solid solution joins (e.g.,Hill et al., 2000; van Westrenen et al., 1999), systematics of heterovalent substitution (Wood and Blundy, 2001) and, in several studies (Blundy et al., 1996; van Westrenen et al., 2001; Wood and Blundy, 1997), incorporation of the effects of melt composition using an approximation to melt thermodynamics based on ideal mixing of quasi-crystalline six-oxygen species.

There are numerous reports of melt influence on partitioning behavior (e.g., Kohn and Schofield, 1994; Linnen and Keppler, 2002; Mysen and Virgo, 1980; Peters et al., 1995; Prowatke and Klemme, 2005). Recent work on the importance of melt composition has focused on the polymerization state of the melt, a melt structure index, as a key variable (e.g., Libourel, 1999; Mysen and Dubinsky, 2004; Toplis and Corgne, 2002). Because the magnitude and complexity of interactions among variables in natural systems often obscure their relationships to one another, insights sometimes must first come from study of simpler systems. The basalt analogue CMAS ($CaO-MgO-Al_2O_3-SiO_2$) provides a petrologically useful, low-variance system in which to gain fundamental understanding of phase composition influence on partitioning behavior. For our purposes, the key advantages of the CMAS system are the purity of mineral phases that crystallize in this system and the availability of a high-quality activity-composition model for the melt phase at ambient pressure (Berman, 1983). Together, these advantages allow us to isolate the role of melt composition in variation of partition coefficients and to separate these variations into the part that can be understood through the major-element thermodynamics of crystal-liquid equilibrium and the residual part that reflects behavior of trace elements in the melt.

We isolate the effects of melt composition on divalent element (Mg, Ca, Sr, and Ba) partitioning between anorthite and a range of seven CMAS liquid compositions. We chose anorthite because it crystallizes from a wide range of melt compositions in CMAS, and because in Na-free systems we expected essentially no variation in mineral composition. This work considers how abundance of major element network-modifying cations, Ca and Mg, in nearly isopolymerized melts controls partitioning of alkaline earth

elements, which are cations of moderate charge density and not expected to exhibit much variation in D_i values (Ryerson and Hess, 1978; Watson, 1976). The systematic variation in the parameter D_o that we observe in our experimental systems is thermodynamically rationalized in terms of major element melt chemistry. Remaining deviation in partitioning behavior from the best-fitting lattice strain model, after this major-element melt thermodynamics correction, is taken to represent the influence of melt trace species activities. Although the particular example shown here is restricted to the CMAS system, it is meant to illustrate how, in general, the availability of an activity-composition model for multi-component melts, in combination with lattice strain theory and some corrections for trace activities in the melt, leads to a general theory for prediction of partition coefficients.

2.2 DESIGN CONSIDERATIONS

2.2.1 Choice of Compositions

Given that crystal chemistry likely controls the bulk of isovalent trace element mineral/melt partitioning variation (Blundy and Wood, 1994), the challenge of isolating the influence of melt composition lies in varying melt composition while keeping mineral composition constant from experiment to experiment, at constant temperature and pressure. We sought to achieve this by identifying melt compositions in the simple CMAS system, using an internally consistent thermodynamic model (Berman, 1983), that are expected to coexist with stoichiometric anorthite at our chosen liquidus temperature of 1400 °C. These criteria amount to two nonlinear constraints on the choice of liquid

compositions, which reduces the three degrees of compositional freedom in this quaternary system to one. First, in order to have equal liquidus temperature, all the compositions must satisfy the equilibrium

$$CaAl_2Si_2O_{8\,An} = CaO_{\,melt} + Al_2O_{3\,melt} + 2SiO_{2\,melt} \qquad (2.2)$$
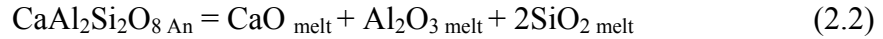
at equal temperature. Applying the law of mass action, the equilibrium constant for this reaction is

$$K^{fusion}_{anorthite} = \frac{\left(a^{CaO}_{melt}\right)\left(a^{Al_2O_3}_{melt}\right)\left(a^{SiO_2}_{melt}\right)^2}{a^{CaAl_2Si_2O_8}_{plagioclase}}. \qquad (2.3)$$

Hence all liquids that coexist with nearly pure anorthite ($a^{An}_{plag} = 1$) at given conditions have equal values of the activity product $(a_{CaO})(a_{Al2O3})(a_{SiO2})^2$.

Second, anorthite is known to incorporate significant amounts of excess silica ($[]Si_4O_8$) into its structure under low-pressure experimental conditions (Bruno and Facchinelli, 1974; Ito, 1976; Longhi and Hays, 1979) and in some natural environments both terrestrial (Bryan, 1974; Kimata et al., 1995; Murakami et al., 1992) and lunar (e.g., Beaty and Albee, 1980; Bruno and Facchinelli, 1975). Attempts to use starting melt compositions ranging from 45 to 65 wt % SiO_2 and constant 1 wt % MgO content generated crystals with a wide range of mole fractions of the excess silica component. As a result, any melt composition contribution to partitioning behavior in these experiments could not be readily resolved from the effect of significant changes to the crystal structure resulting from solid solution with SiO_2. Hence, in order to find compositions that would crystallize anorthite of identical stoichiometry, we write the substitution reaction for excess SiO_2 in anorthite:

$$CaAl_2Si_2O_{8\,plag} + 2SiO_{2\,melt} = CaO_{melt} + Al_2O_{3\,melt} + [\ ]Si_4O_{8\,plag}. \qquad (2.4)$$
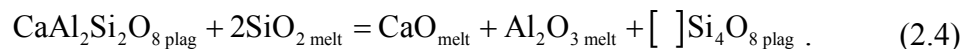
The equilibrium constant for this reaction is

$$K_{\text{plagioclase}}^{\text{exchange}} = \frac{\left(a_{\text{melt}}^{\text{CaO}}\right)\left(a_{\text{melt}}^{\text{Al}_2\text{O}_3}\right)\left(a_{\text{plag}}^{[\ ]\text{Si}_4\text{O}_8}\right)}{\left(a_{\text{plag}}^{\text{CaAl}_2\text{Si}_2\text{O}_8}\right)\left(a_{\text{melt}}^{\text{SiO}_2}\right)^2} \, ,$$

(2.5)

which shows that, at equal temperature, all melt compositions with equal value of the activity quotient $(a_{\text{CaO}})(a_{\text{Al2O3}})/(a_{\text{SiO2}})^2$ should yield anorthite compositions with equal activity of the excess silica component.

From our family of solutions that fit these two constraints (a curvilinear subspace of CaO-MgO-Al_2O_3-SiO_2 space), we selected seven points that would span the range of possible melt compositions yet still lie comfortably within the anorthite phase volume, to ensure that no other phases would crystallize during controlled cooling experiments. Figure 2.1 illustrates the locations of these compositions within the CMAS tetrahedron.
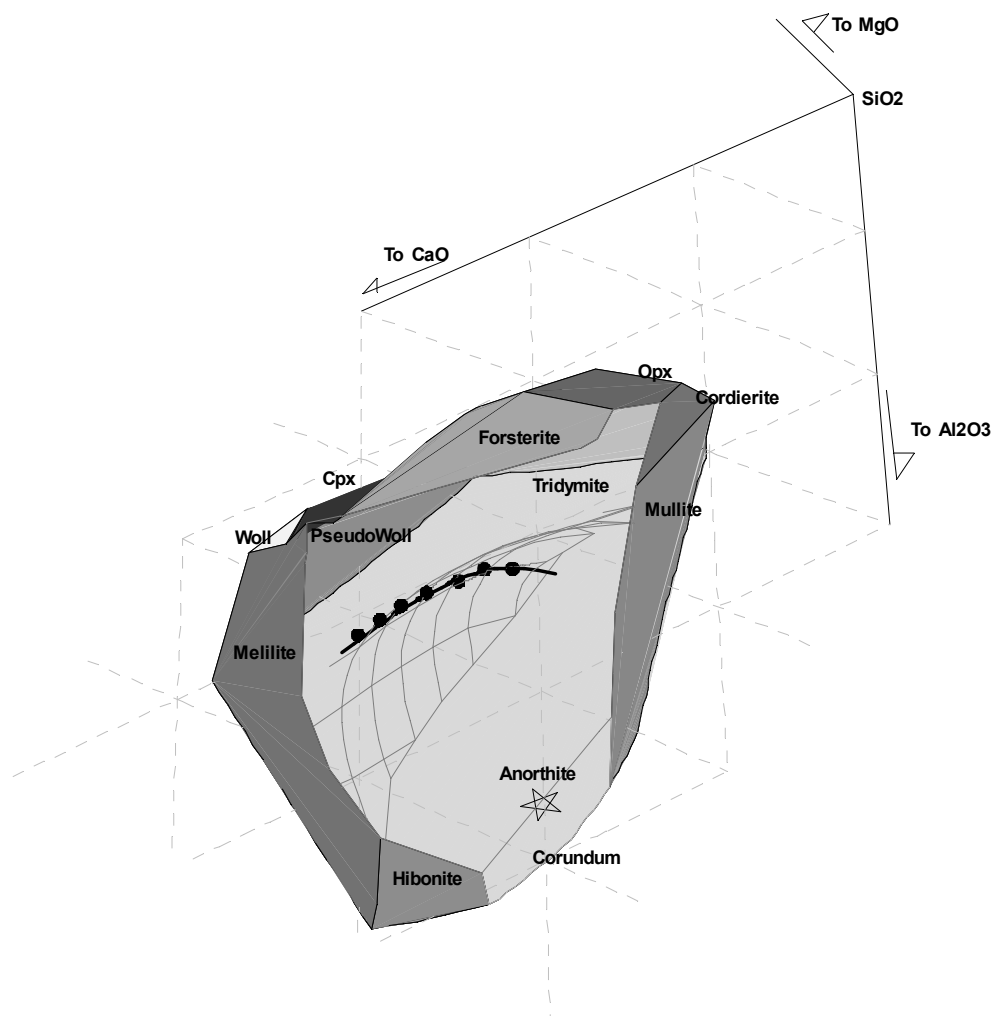
Figure 2.1. The choice of liquid compositions for this study is illustrated in a three-dimensional perspective view of the CMAS tetrahedron. The composition of anorthite is shown by the black star. The anorthite liquidus volume is delimited by the CAS ternary base and a number of bounding surfaces, each labeled by the phase that coexists with anorthite and liquid on that boundary; the spinel boundary has been left transparent to expose the interior of the phase volume. Within that volume, the gray mesh surface indicates the 1400 °C isotherm on the liquidus, calculated using the Berman (1983) model. The black contour on this surface shows the range of liquid compositions that are expected to crystallize stoichiometric anorthite without excess silica (see text). The points along the black contour indicate the seven compositions chosen to span the maximum compositional range consistent with the constraints of crystallizing stoichiometric anorthite at 1400 °C.

2.2.2 Choice of Experimental Protocol

In designing our experimental protocol, we needed to make a basic choice between constant-temperature equilibrium crystallization and controlled-cooling rate fractional crystallization. For the reasons detailed below, we decided that controlled-cooling rate fractional crystallization experiments are more feasible in this system than any attempt to reach static equilibration at constant conditions. Diffusion studies of divalent elements Mg, Ca, Sr, and Ba in plagioclase indicate that diffusion on experimental time scales even at temperatures in excess of 1300 °C is sluggish. Following Cherniak (2002), a spherical approximation of a 100 μm diameter labradorite (An_{67}) grain indicates that it would take six months at 1300 °C for the Ba concentration in the plagioclase core to begin equilibrating with the surrounding melt. Ba diffusion is likely even slower in anorthite than in intermediate plagioclases due to the greater rigidity of calcic plagioclase structures (Blundy and Wood, 1994). Divalent cation diffusion in end-member anorthite is also strongly dependent on ionic radius, with Mg diffusion likely over 200 times faster than that of Ba, according to Mg data of LaTourrette and Wasserburg (1998).

The slow diffusivity of divalent cations within plagioclase makes it ideal for investigating long-term magma chamber evolution using zoning profiles (e.g., Bindeman et al., 1999; Blundy and Shimizu, 1991; Singer et al., 1995), but it presents a significant experimental challenge in equilibrium partitioning studies. On the other hand, assuming that diffusion of these elements in the melt is much faster, the same slow diffusivity

allows nearly perfect fractional crystallization experiments. In light of this, crystal rim trace element compositions were chosen over core data as the most promising representation of equilibrium between anorthite and the coexisting melts of these experiments.

Although a tempting approach would be to calculate partition coefficients based on analysis of core compositions assumed to crystallize first from the starting melt, this introduces a number of unknowns. One disadvantage of relying on core data to capture initial crystallization compositions results from having to assume that, upon nucleating, crystals grow uniformly outward in all directions. In many cases, crystals may nucleate on the surface of the melt bead or on the platinum loop and grow outward from that surface (e.g., Kirkpatrick, 1974; Klein and Uhlmann, 1974; Roskosz et al., 2005; Stolper and Paque, 1986). In these cases, the geometrical centers of the crystals do not crystallize from the initial melt composition. A second disadvantage results from the kinetic barrier of supercooling that prevents crystallization from occurring exactly at the anorthite liquidus temperature of the melt. When crystallization does occur, initial crystallization is likely to be rapid (Lofgren, 1974b) until some degree of kinetic equilibrium is established, after which crystallization progresses at a slower pace, following the controlled cooling pattern established by the thermal program. The initiation of crystallization may also be random, varying from experiment to experiment. Gibb (1974) observed that random nucleation of liquidus phase plagioclase from the Columbia River basalt may occur within a range of over 35 °C below the liquidus. The more recent work of Tsuchiyama (1983) with anorthite and $Di_{50}An_{50}$ melt demonstrates that delay in

anorthite nucleation is a function both of initial superheating above its liquidus and duration of time superheated prior to cooling and crystallization.

In order to avoid crystallizing a myriad of tiny (5−10 μm diameter) anorthite crystals that cannot be analyzed with available instrumentation, runs were heated to 10− 20 °C above the liquidus to dissociate most of the potential nuclei in the starting melt. Controlled cooling of the sample at 2 °C/hour has allowed us over 100 hours to grow anorthite crystals with shortest dimensions in excess of 100 μm, providing ample area for analysis. The regular, tabular morphology of these experimental CMAS anorthite laths attests to initiation of slow, controlled crystallization not far from the liquidus. Lofgren (1974a) demonstrated that plagioclase crystals with tabular morphology generally grow when the degree of supercooling is 30 °C or less in basaltic liquid. At higher degrees of supercooling, acicular and skeletal crystals are formed.

2.2.3 Choice of Doping Concentrations

The choice of a fractional crystallization model and rim compositions to represent the solids requires fairly good spatial resolution, even though the experimental crystals are quite large. This, in turn, makes electron probe analysis in some ways superior to ion probe analysis with the typical performance characteristics of most ion probes. However, analysis of Sr and Ba by electron probe requires doping to fairly high concentration and this, in turn, requires evaluation of the limits of Henry's law behavior. Recent work of Bindeman and Davis (2000) has reconfirmed the results of Drake and Weill (1975), showing partition coefficients of Sr between plagioclase and melts of natural

concentration to be identical to those of synthetic samples doped to 11,000 ppm. Bindeman and Davis also demonstrated similar Henrian behavior of Ba doped at 5500 ppm, and Drake and Weill report Ba exhibiting the same Henry's law constant for melt concentrations in excess of 2 wt. %. As our experiments were doped with approximately 1000 ppm Sr and 3000 ppm Ba, we expect no deviation from Henry's Law for the solid in this concentration range for these elements.

2.2.4 Experimental Procedure and Analytical Methods

Alfa Aesar Puratronic™ SiO_2, Al_2O_3, MgO, and $CaCO_3$ were used to make our starting compositions. Ingredients were dried overnight; the oxides at 800 °C and $CaCO_3$ at 140 °C. Materials were removed from the drying oven and cooled in vacuum before weighing. Weighed quantities were ground under ethanol in an alumina mortar for five hours. After drying, each mixture was decarbonated by heating to 1000 °C in 200 °C/hour steps and remained at 1000 °C for 24 hours. Powdered mixtures were fused in Pt crucibles at 1450 °C and reground under ethanol for one hour. Half gram separates were spiked with Ba and Sr solutions to achieve concentrations of 3000 ppm and 1000 ppm, respectively, dried, re-fused at 1450 °C, and reground for half an hour. After both grinding steps the fine powder contained a mixture of glass fragments ranging from <1 μm to ~50 μm.

All experiments were conducted at 1 atm in a Deltech vertical muffle furnace. Reconnaissance experiments have shown that anorthite crystals may gain as much as 4 mol % albite component over the course of a 100-hour run in stagnant air. Therefore,

we ran a flow of compressed air through the muffle tube in excess of 200 cm^3/hour to minimize the partial pressure of sodium. Temperatures were monitored by a type S Pt-Pt$_{0.9}$Rh$_{0.1}$ thermocouple. Each experimental charge consisted of ~30 mg of starting material adhered with polyvinyl alcohol to Pt wire loops suspended from a wheel-shaped sample hanger fashioned from 0.5 mm diameter Pt wire.

The thermal history of the experiments was adapted from Simon et al. (1994). Samples of the seven compositions were run in the furnace simultaneously to ensure identical temperature and pressure conditions. After allowing the powder pellets to dry at room temperature for a minimum of six hours, the charges were lowered into the furnace and a multi-step controlled temperature program was begun. First the temperature was raised to approximately 10 °C above the median liquidus of the seven compositions. The furnace was held at that temperature for one hour to reduce the number of potential crystal nuclei in the melts. Next the temperature was decreased 2 °C/hour to 25 °C below the median liquidus and held at constant temperature for 24 hours to allow any rapidly growing crystals to catch up with the thermal conditions and to compensate for delayed nucleation. Cooling then continued at 2 °C/hour to the final hold temperature of 1330 °C. Charges remained at the final run temperature for 30 hours. The samples were quenched by removal out of the top of the furnace and dipping in distilled water.

Samples were mounted in Araldite epoxy and cross sectional surfaces were polished to 0.3 μm fineness with alumina. Element compositions were analyzed using the Caltech JEOL JXA-733 electron microprobe, and raw data were reduced using the CITZAF correction procedure (Armstrong, 1988). Standards used were albite, microcline, fayalite, anorthite, forsterite, a Sr-silicate glass, and benitoite (for Ba). Beam

conditions of 25nA and 15 keV with a 10 μm defocused beam were used for collecting major element data. Counting times were 30 s on-peak and 15 s for each background measurement. Sr, Ba, and Mg in anorthite were also analyzed at 400 nA and 15 keV with a focused beam for 90 s on-peak and 45 s per background. One-sigma (1σ) analytical uncertainty ($\sqrt{N}$) for a given point is <2% relative for Sr, Ba, and Mg at operating conditions and counting times specified for both phases. Secondary electron imaging of the 400 nA focused beam spots show the resulting burn marks in the carbon coat to be no more than 12 μm in diameter.

In order to identify any zoning in the crystals, we analyzed rim-to-rim polygonal grids of 100–200 points in 7–9 μm steps oriented in the centers of the long dimension of crystals. Major element compositions were uniform but trace elements showed normal zoning (i.e., concentration increasing towards rim) in some cases. Partitioning analysis and crystal data presented below use only rim analyses most likely to be in equilibrium with the coexisting melt at the final hold temperature of 1330 °C. Although the constraint that each liquid composition should coexist with stoichiometrically identical anorthite in all seven charges was applied at an anorthite liquidus temperature of 1400 °C, rim-to-rim transects across crystals from each indicate no significant major element variability for crystal edges formed at lower temperature. This permits us to treat crystal chemistry as constant and compare anorthite rim data between charges.

2.2.5 Rates of Crystal Growth and Possible Nonequilibrium Enrichment

In order to place some constraints on the rates of crystal growth, separate runs were conducted in which charges were quenched at intermediate temperatures along the controlled cooling path of these experiments. Extents of crystallization were calculated from the Rayleigh equation and glass major element compositions. The bulk of crystal growth occurs between 45 and 67 hours into our runs, when temperature decreases from 1380 °C to the final temperature of 1330 °C. The most magnesian liquid composition (2b-7) produces the greatest increase in volume crystallized over this interval: from approximately 6 % crystallized to 27 %. For all compositions the fraction crystallized remains constant within analytical error during the final 30 hours of the thermal history in which the charges are held at the final temperature. This indicates that rim growth is unlikely to be affected by supercooling at this stage of the experiments.

How closely our experiments approximate equilibrium partitioning between anorthite and melt depends on how quickly the cations of interest can diffuse away from the crystal interface into the bulk melt, relative to the crystal growth rate. If the anorthite crystallizes faster than diffusion can restore compositional homogeneity throughout the melt, a concentration gradient will develop around the growing crystal. In this rapid growth scenario, incompatible trace elements will become enriched in the melt boundary layer and be incorporated into the expanding crystal structure in greater concentrations than would be characteristic of equilibrium partitioning between the crystal interface and the melt as a whole.

Even if cation diffusion within the melt is rapid enough to prevent buildup of a liquid concentration gradient in incompatible elements, crystal zoning can occur if the growing crystal incorporates incompatible elements from the melt more quickly than those cations can diffuse out of the moving boundary layer (a few unit cells thick) of the anorthite crystals themselves. The sector zoning model of Watson and Liang (1995) demonstrates how this can occur even in instances of slow growth, such as titanite formation within plutons, if temperatures are low (700–800 °C) and cation diffusivities through the crystal lattices are slow. Possible extent of non-equilibrium surface enrichment in the experimentally grown anorthites of this study may be evaluated using the general, qualitative version of the Watson and Liang model. In it they assume that the half width of a crystal growth layer is a 5 Å silicate monolayer, and that the lattice diffusion distance is approximately equal to the growth distance into the melt when V/Df_i $\approx 2 \cdot 10^9$ m^{-1}, where V is the growth rate (m/s) and Df_i is the lattice diffusivity of element i (m^2/s). Surface enrichment is likely to be preserved within the crystal structure if $V \geq 2 \cdot 10^9 \, Df_i$.

To obtain a conservative estimate for the fastest rate of crystal growth in the experiments of this study, one may calculate the total volume a sample melt bead from its quenched diameter of 3 mm. We consider this melt volume as a cube with half-edge length 1.2 mm and represent a change from 6 % to 27 % crystal growth as an expansion of a single theoretical cubic lath of anorthite from the center of the melt cube. Assuming crystal and melt have roughly comparable densities and isotropic growth, the one-dimensional growth outward in any direction parallel to the faces of this melt cube between 6 % and 27 % crystallization is ~310 μm. Assuming crystal growth follows the

linear progression of the controlled cooling of the furnace from ~1380 to 1330 °C, the crystal growth rate of this theoretical anorthite cube is ~ $4 \cdot 10^{-9}$ m/s.

This simple calculation represents an upper limit on growth rate, as anorthite typically forms rectangular laths, and growth at later stages onto an existing crystal will build width in layers parallel to the elongated direction of the crystal, requiring the growth rate along that width to be slower for a given volume increase than if the crystal had a cubic shape. Furthermore, assuming multiple crystals nucleate within a charge instead of one lone crystal in the above thought experiment, comparable increases in overall crystal volume will occur with any given crystal having a proportionally smaller width than it would have in the single crystal scenario. Thus the short length of a crystal analyzed in our experiments, which average between 5 and 20 exposed crystal cross sections per charge, is likely the result of a lower growth rate than that calculated for a hypothetical solitary crystal.

The competition between crystal growth rate and lattice diffusion in determining whether or not surface enrichment develops also depends on knowledge of cation diffusion in anorthite at temperatures of interest. According to the first-order, qualitative version of the Watson and Liang model and the estimate of anorthite growth rate given above, surface enrichment might be expected if lattice diffusion for cations of interest is slower that $2 \cdot 10^{-18}$ m^2/s, according to our upper bound crystal growth rate. Calculating the diffusivity of Sr in anorthite at 1330 °C using the Arrhenius parameters of Giletti and Casserly (1994) yields a value of $1.14 \cdot 10^{-17}$ m^2/s, which is about an order of magnitude faster than our surface enrichment threshold.

No data exist for Ba diffusion in pure anorthite, and diffusion rates may be higher in more albitic compositions. The most anorthitic plagioclase composition (An_{67}) of the Cherniak (2002) study, along its slowest direction, perpendicular to (001), has a Ba diffusivity at 1300 °C of $7 \cdot 10^{-18}$ m^2/s. The proximity of this value to our surface enrichment threshold may mean that there is a higher probability that the observed Ba content of anorthite rims in this study are elevated above equilibrium values, but our approximation of crystal growth and knowledge of diffusion behavior in these experiments are too uncertain to constrain this further.

2.3 RESULTS AND DISCUSSION

2.3.1 Anorthite-Melt Partitioning Data

Melt and anorthite compositions are listed in Tables 2.1 and 2.2, respectively. Liquidus temperatures (Table 2.3) of the starting materials were determined from isothermal experiments in which samples were lowered into the furnace at desired run temperature and removed after three hours. Presence or absence of crystallization was ascertained by visual inspection. Mass balance calculations of charge compositions indicate that anorthite is the sole crystal phase present in all experiments and extent of crystallization ranges from 15 % to 30 %. Because the percent crystallization of anorthite was relatively low in these experiments, the melt composition upon quenching did not deviate far enough from the starting liquid to produce identifiable changes in anorthite major element chemistry.

Table 2.1. Compositions of melt quenched to glass (wt. %) coexisting with anorthite at 1330 °C determined by EMP. Uncertainties (1σ) for the last digit(s) indicated in parentheses.

	2b-1-2 n = 10 Mg,Sr,Ba n = 17	2b-2-2 n = 10 Mg,Sr,Ba n = 27	2b-3-2 n = 10 Mg,Sr,Ba n = 7	2b-4-2 n = 10 Mg,Sr,Ba n = 9	2b-5-2 n = 10 Mg,Sr,Ba n = 16	2b-6-2 n = 10 Mg,Sr,Ba n = 21	2b-7-2 n = 10 Mg,Sr,Ba n = 23
SiO_2	47.97 (11)	47.41 (30)	47.86 (9)	47.60 (28)	46.34 (29)	46.29 (29)	46.39 (13)
Al_2O_3	18.14 (19)	17.80 (14)	17.92 (16)	18.03 (8)	18.80 (7)	19.83 (12)	20.97 (6)
MgO	1.19 (6)	3.22 (1)	5.52 (5)	7.76 (1)	10.28 (3)	12.52 (6)	14.66 (30)
CaO	32.48 (18)	30.68 (14)	28.05 (10)	25.86 (11)	23.20 (8)	20.25 (5)	17.57 (10)
SrO	0.136 (5)	0.144 (4)	0.142 (6)	0.133 (6)	0.141 (5)	0.147 (4)	0.127 (4)
BaO	0.60 (3)	0.64 (1)	0.65 (1)	0.66 (1)	0.73 (1)	0.71 (1)	0.72 (2)
FeO*	0.06 (1)	0.07 (1)	0.08 (2)	0.07 (1)	0.07 (3)	0.10 (1)	0.07 (2)
K_2O	0.021 (6)	0.019 (7)	na	0.026 (7)	0.023 (5)	na	na
Na_2O	0.01 (1)	0.02 (1)	0.02 (1)	0.02 (1)	0.02 (1)	0.02 (1)	0.02 (1)
	100.62(18)	100.02(30)	100.25(18)	100.15(19)	99.61(25)	99.87(16)	100.52(34)

* All Fe reported as FeO
na = not analyzed

Table 2.2. Anorthite compositions (wt. %) coexisting with melt at 1330 °C determined by EMP. Uncertainties (1σ) for the last digit(s) indicated in parentheses.

	2b-1-2 n = 10 Mg,Sr,Ba n = 19	2b-2-2 n = 10 Mg,Sr,Ba n = 11	2b-3-2 n = 10 Mg,Sr,Ba n = 10	2b-4-2 n = 10 Mg,Sr,Ba n = 6	2b-5-2 n = 10 Mg,Sr,Ba n = 8	2b-6-2 n = 10 Mg,Sr,Ba n = 9	2b-7-2 n = 10 Mg,Sr,Ba n = 12
SiO_2	43.41 (10)	43.04 (23)	43.39 (12)	43.45 (26)	42.98 (18)	43.09 (44)	43.46 (20)
Al_2O_3	36.48 (15)	35.92 (10)	36.21 (11)	35.99 (6)	35.52 (8)	35.92 (29)	36.20 (10)
MgO	0.099 (4)	0.226 (4)	0.298 (7)	0.359 (28)	0.376 (6)	0.371 (11)	0.376 (12)
CaO	20.38 (11)	20.41 (10)	20.28 (6)	20.39 (9)	20.30 (5)	20.12 (7)	20.05 (10)
SrO	0.111 (5)	0.120 (5)	0.123 (5)	0.109 (14)	0.144 (5)	0.166 (4)	0.160 (5)
BaO	0.097 (8)	0.086 (12)	0.092 (6)	0.126 (4)	0.117 (7)	0.115 (6)	0.133 (14)
FeO*	0.02 (2)	0.01 (1)	0.03 (1)	0.02 (1)	0.02 (2)	0.02 (1)	0.02 (1)
K_2O	0.020 (7)	0.016 (6)	na	0.018 (6)	0.017 (5)	na	na
Na_2O	0.01 (1)	0.02 (1)	0.01 (1)	0.02 (1)	0.02 (1)	0.02 (1)	0.02 (1)
	100.63 (41)	99.85 (48)	100.43 (33)	100.48(45)	99.49 (36)	99.82 (84)	100.42 (45)

* All Fe reported as FeO
na = not analyzed

Anorthite crystals exhibit tabular, lath-like morphology. A few appear to contain melt inclusions and such crystals were avoided during analysis. Figure 2.2 shows a

representative sample cross-section from these experiments. No identifiable quench textures were formed in the charges. Linear transects extending perpendicularly in 2 μm steps from crystal rims to ~70 μm into surrounding melt revealed only slight concentration gradients for Mg in the most magnesian composition, and none for Ba and Sr even in samples quenched at 67 hours, immediately after the 2 °C/hr cooling step at the final hold temperature of 1330 °C. This indicates that near-equilibrium conditions were likely reached, although the most conservative interpretation is that all calculated partition coefficient data from this study should be considered upper limits (assuming kinetic effects will enrich growing crystals in incompatible trace elements and produce elevated D values).
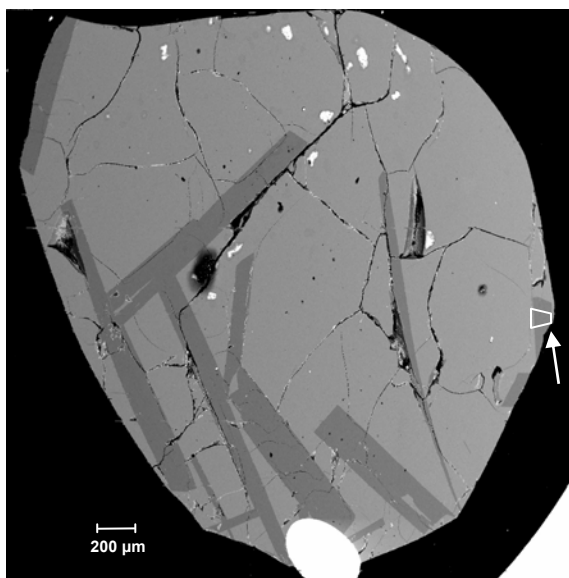

Figure 2.2. Back-scattered electron image of sample 2b-3-2. Crystals showing rapid growth and/or melt inclusions were avoided in analysis. Analyzed polygonal grid area outlined in white and indicated by arrow.

Divalent element partition coefficients between anorthite and coexisting melt at time of sample quenching (Table 2.3) show a systematic decrease in the observed bulk Mg partition coefficient as melts become more magnesian, and similarly, Ca partition coefficients have lower values with increasing lime content in coexisting liquids. D_{Sr} increases with increasing D_{Ca}. D_{Ba}, though analytically less resolved, indicates a corresponding trend of higher partition coefficient with lower calcium abundance in melt.

Table 2.3. Normalized CMAS melt compositions (wt. %) and molar partition coefficients with 1σ uncertainties for the last digit(s) indicated in parentheses. Molar partition coefficients calculated from EMP weight % data as neutral oxides: (moles XO/g)/Σ(moles XO/g) in anorthite divided by the same quantity in the glass. Uncertainty of anorthite liquidus temperatures is $\sim\pm5$ °C. NBO/T and optical basicity (O.B.) are calculated according to Mills (1993) from full melt composition data. D^{molar}_{MgVIII} calculated from equation (2.17) using the reoptimized parameters listed in chapter 3.

	2b-1	2b-2	2b-3	2b-4	2b-5	2b-6	2b-7
T_{Liq} (°C)	1398	1402	1400	1408	1408	1408	1403
CaO	32.55 (18)	30.96 (14)	28.23 (10)	26.06 (11)	23.52 (8)	20.48 (5)	17.64 (10)
MgO	1.19 (6)	3.25 (1)	5.56 (5)	7.82 (1)	10.42 (3)	12.66 (6)	14.72 (30)
Al_2O_3	18.18 (19)	17.96 (14)	18.04 (16)	18.17 (8)	19.06 (7)	20.05 (12)	21.06 (6)
SiO_2	48.08 (11)	47.84 (30)	48.17 (9)	47.96 (28)	46.99 (29)	46.81 (29)	46.58 (13)
NBO/T	0.749 (6)	0.799 (7)	0.803 (6)	0.834 (7)	0.853 (6)	0.826 (8)	0.799 (10)
O.B.	0.618 (3)	0.617 (4)	0.613 (4)	0.612 (4)	0.611 (4)	0.607 (4)	0.603 (4)
D^{molar}_{Mg}	0.091 (5)	0.077 (1)	0.061 (1)	0.052 (4)	0.042 (1)	0.034 (1)	0.029 (1)
D^{molar}_{MgVIII}	0.0024	0.0023	0.0026	0.0029	0.0035	0.0049	0.0067
D^{molar}_{Ca}	0.689 (5)	0.738 (4)	0.805 (3)	0.886 (5)	0.993 (4)	1.134 (4)	1.309 (9)
D^{molar}_{Sr}	0.90 (5)	0.92 (4)	0.97 (5)	1.06 (5)	1.16 (5)	1.29 (4)	1.45 (6)
D^{molar}_{Ba}	0.18 (2)	0.15 (2)	0.16 (1)	0.18 (2)	0.18 (1)	0.19 (1)	0.21 (2)

2.3.2 Thermodynamic Modeling

The data can be thermodynamically rationalized by using oxide exchange and mineral fusion reactions, an approach common in the literature(e.g.,Beckett and Stolper, 2000; Drake, 1976; Drake and Weill, 1975; Longhi et al., 1976), to predict cation partitioning behavior. To demonstrate, we consider an exchange reaction for Ba^{2+} partitioning into anorthite using neutral species and oxide-mineral exchange:

$$BaO_{melt} + CaAl_2Si_2O_{8 anorthite} = CaO_{melt} + BaAl_2Si_2O_{8 anorthite} \ . \tag{2.6}$$
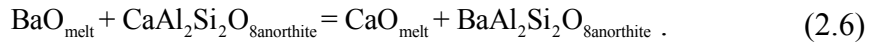
The energy associated with this thermodynamic mixing contribution can be understood in terms of the reaction equilibrium constant,

$$K_{anorthite}^{exchange} = e^{(\Delta G_{exchange}^o / RT)} = \frac{a_{melt}^{CaO} \, a_{anorthite}^{BaAl_2Si_2O_8}}{a_{melt}^{BaO} \, a_{anorthite}^{CaAl_2Si_2O_8}} \ . \tag{2.7}$$

The equations for the reaction of fusion of the end-member host anorthite and corresponding equilibrium constant are:

$$CaO_{melt} + Al_2O_{3\,melt} + 2\,SiO_{2\,melt} = CaAl_2Si_2O_{8\,anorthite} \ , \tag{2.8}$$
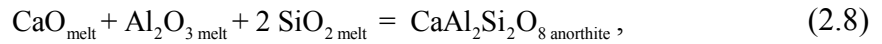
$$K_{anorthite}^{fusion} = e^{(\Delta G_{fusion}^o / RT)} = \frac{a_{anorthite}^{CaAl_2Si_2O_8}}{a_{melt}^{CaO} \, a_{melt}^{Al_2O_3} \, (a_{melt}^{SiO_2})^2} \ . \tag{2.9}$$

Multiplication of the fusion and exchange equilibrium constants for anorthite yields

$$\frac{a_{anorthite}^{BaAl_2Si_2O_8}}{a_{melt}^{BaO}} = a_{melt}^{Al_2O_3} \, (a_{melt}^{SiO_2})^2 \, e^{[(\Delta G_{fusion}^o + \Delta G_{exchange}^o) / RT]} \ . \tag{2.10}$$

Explicit incorporation of BaO activity coefficients in both the melt and solid phases produces an expression for the molar partition coefficient of the trace element:

$$D_{BaO}^{anorthite/melt} = \frac{X_{anorthite}^{BaAl_2Si_2O_8}}{X_{melt}^{BaO}} = \frac{\gamma_{melt}^{BaO}}{\gamma_{anorthite}^{BaAl_2Si_2O_8}} a_{melt}^{Al_2O_3} (a_{melt}^{SiO_2})^2 e^{[(\Delta G_{fusion}^o + \Delta G_{exchange}^o)/RT]} . \quad (2.11)$$

Such treatment differs from the analysis of other studies (Blundy et al., 1995; van Westrenen et al., 2001; Wood and Blundy, 1997) by applying a calibrated, oxide-based non-ideal melt mixing model that explicitly describes the D_o term of equation (2.1) as an activity product, rather than relying on an ideal quasi-crystalline melt model where careful selection of speciation and exchange reactions is meant to approximate liquid influence on partitioning. Given that little thermodynamic data for possible melt species exist, particularly for those involving trace elements, the approach preferred here offers a potentially more rigorous accounting of melt thermodynamics when precise experimental data and access to a sufficiently well-calibrated melt model permit.

2.3.3 Equilibrium and CMAS melt model tests

Before proceeding to use these data to extend the lattice strain model of trace element partitioning from an oxide melt perspective, we can perform some tests of whether our data are consistent with near-equilibrium conditions and whether the fusion and exchange relationships described in the previous section are consistent with observed partitioning behavior. We calculate the activities and activity coefficients in the melt based on Berman's (1983) 1 atm stoichiometric model of CMAS liquids. This model uses simple neutral oxides as species and parameterizes melt activities for each oxide as a function of composition and temperature with enthalpy and entropy excess mixing terms (Margules parameters) fitted to mineral-melt equilibria, liquidus, and calorimetric data.

Because the reported uncertainty in the anorthite liquidus temperature for the 20 wt. % Al_2O_3 plane of the quaternary (near our region of interest) exceeds 20 °C, a reoptimization of the Berman model was performed for a portion of the anorthite liquidus space. This was accomplished by adjusting the Margules parameters to minimize the differences between the liquidus temperatures predicted by the model and those experimentally determined for anorthite in 57 CMAS liquids with SiO_2 content between 40 and 50 wt. % (this study, Osborn, 1942; Osborn and Tait, 1952; Tsuchiyama, 1983; Yang et al., 1972). Reoptimization decreased the sum of the discrepancies squared between the observed and predicted liquidus temperatures by 35 %. Results of the anorthite field parameterization used are reported in chapter 3; we caution that this re-optimization considered only anorthite-melt constraints and is presumed to be worse than the original Berman model at describing equilibria with other solids.

For a given trace element obeying Henry's law in anorthite at equilibrium conditions in our experiments, we would expect that its activity coefficient in anorthite would be constant for all melt compositions; of course the standard state quantities ΔG^o_{fusion} and $\Delta G^o_{exchange}$ are also constants at given temperature (see equation (2.11)). We cannot perform this test using Sr or Ba data because the Berman model does not provide activities of these components in the melt. For Ca, this relationship tests only whether the re-optimized Berman model accurately predicts liquidus temperatures. Hence Mg, the only component of the Berman CMAS melt model that enters the anorthite structure as a trace constituent, provides the best test, but it is complicated by the possibility of substitution into two different sites. Although technically the M-site of anorthite (where Ca resides) has VII-fold coordination, here it will be referred to as VIII-coordinated since

the ionic radius data of Shannon (1976) used later in this paper does not include VII-coordinated Mg radii. This convention also allows us to more easily compare our results to previous work (Blundy and Wood, 1994), which used VIII-fold coordinated ionic radii for divalent elements substituting into plagioclase. The decision to use VIII-fold rather than VII-fold coordinated ionic radii introduces an average 0.06 Å shift in r_o but has no effect on the overall conclusions drawn from this study.

If all Mg were to substitute onto the VIII-fold site of the anorthite structure, our model would predict that the relationship between $D^{molar}_{MgO}/a_{Al2O3}(a_{SiO2})^2$ and γ_{MgO} of corresponding melts would be linear and pass through the origin:

$$\frac{D^{molar}_{MgO}}{a^{Al_2O_3}_{melt}(a^{SiO_2}_{melt})^2} = \gamma^{MgO}_{melt}\left(\frac{e^{(\Delta G^o_{fuions}+\Delta G^o_{exchange})/RT}}{\gamma^{MgO}_{plagioclase}}\right). \qquad (2.12)$$

Such a relationship is not found for our re-optimized model and the partitioning data.

Considerable evidence, however, suggests that the majority of Mg in plagioclase resides in a tetrahedrally coordinated (IV) site (e.g., Longhi et al., 1976; Peters et al., 1995), perhaps via an Al substitution. The observed D^{molar}_{MgO} is therefore a sum of partitioning onto both M (i.e., VIII-coordinated) and T (IV-coordinated) sites:

$$D^{molar,observed}_{MgO} = D^{molar,VIII}_{MgO} + D^{molar,IV}_{MgO}. \qquad (2.13)$$

To account for substitution onto the tetrahedral site, we write the appropriate exchange reaction and equilibrium constant expression:
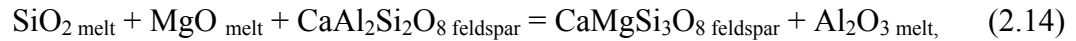
$$SiO_{2\,melt} + MgO_{\,melt} + CaAl_2Si_2O_{8\,feldspar} = CaMgSi_3O_{8\,feldspar} + Al_2O_{3\,melt,} \qquad (2.14)$$

$$K^{exchange}_{feldspar} = e^{(\Delta G^o_{exchange}/RT)} = \frac{a^{Al_2O_3}_{melt}\,a^{CaMgSi_3O_8}_{feldspar}}{a^{MgO}_{melt}\,a^{SiO_2}_{melt}\,a^{CaAl_2Si_2O_8}_{anorthite}}. \qquad 2.15)$$

Multiplication by the anorthite fusion equilibrium constant expression, equation (2.9) generates an equation for partitioning of Mg onto the tetrahedral site:

$$D_{MgO}^{IV} = \frac{\gamma_{melt}^{MgO}}{\gamma_{feldspar}^{CaMgSi_3O_8}} a_{melt}^{CaO} (a_{melt}^{SiO_2})^3 e^{[(\Delta G_{fusion}^o + \Delta G_{exchange,IV}^o)/RT]}. \quad (2.16)$$

This treatment predicts that the observed D_{MgO} for our experiments divided by the melt product $\gamma_{MgO}a_{Al2O3}(a_{SiO2})^2$ for each composition will plot as a linear function of the melt activity quotient $a_{CaO}a_{SiO2}/a_{Al2O3}$ with y-intercept related to the constants for VIII-site partitioning and slope related to the constants for IV-site partitioning:

$$\frac{D_{MgO}}{\gamma_{melt}^{MgO} a_{melt}^{Al_2O_3} (a_{melt}^{SiO_2})^2} = \left[\frac{e^{[(\Delta G_{fusion}^o + \Delta G_{exchange,VIII}^o)/RT]}}{\gamma_{anorthite}^{CaAl_2Si_2O_8}} \right] + \left[\frac{e^{[(\Delta G_{fusion}^o + \Delta G_{exchange,IV}^o)/RT]}}{\gamma_{feldspar}^{CaMgSi_3O_8}} \right] \frac{a_{melt}^{CaO} a_{melt}^{SiO_2}}{a_{melt}^{Al_2O_3}} \quad (2.17)$$
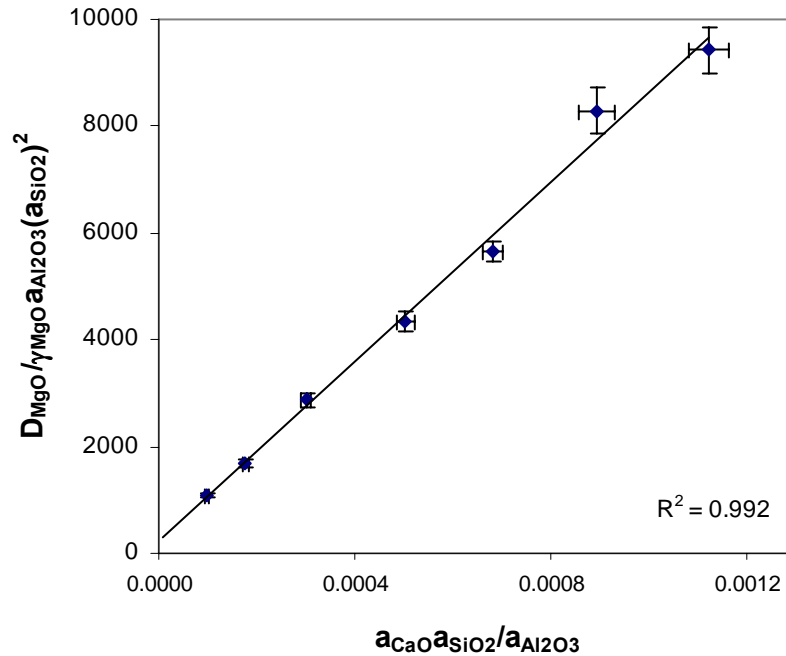

Figure 2.3. Linear relationship of observed $D^{molar}{}_{MgO}$ and melt activity products expected for Mg^{2+} partitioning onto IV and VIII coordination sites of anorthite crystal lattice. Error bars (1σ) for activity products are propagations of activity uncertainties due to

uncertainty in composition values. No estimate is made of systematic errors inherent in the activity model.

Our data as plotted in Figure 2.3 are consistent with these predictions. This suggests that the Mg data are consistent with equilibrium partitioning according to our reoptimized Berman model and, furthermore, allows us to define the distribution of Mg between IV- and VIII-coordinated sites in anorthite. Calculations using reoptimized Berman liquid model oxide activities show how Mg site occupancy at constant anorthite composition varies as a function of melt composition. Sensitivity of such calculations to activity modeling is demonstrated in Figure 2.4, where both the Berman model and its reoptimization in this study are used to calculate Mg site distribution according to equation (2.17).
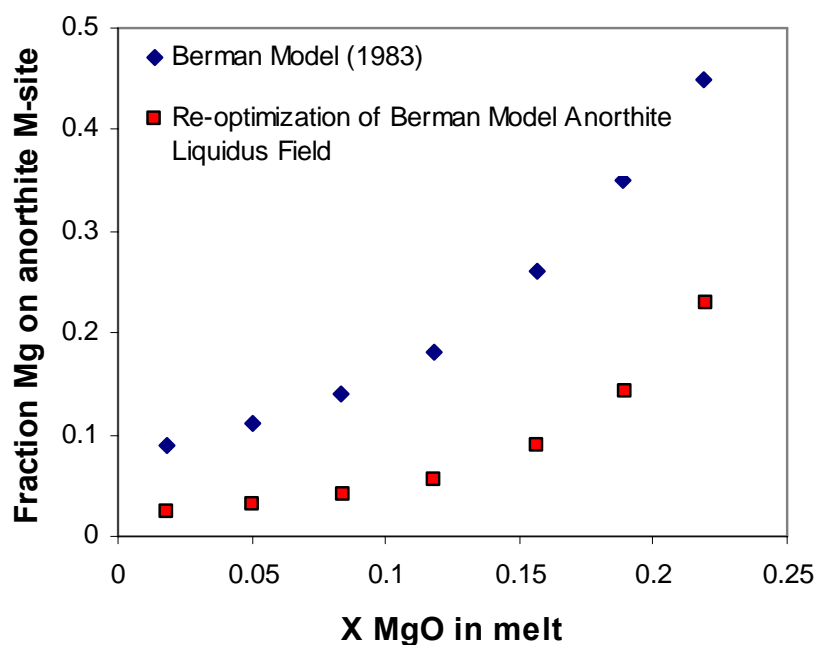

Figure 2.4. Prediction of Mg fractionation between IV (T) and VIII (M) sites in anorthite according to two CMAS liquid activity models: diamonds represent calculation using the Berman (1983) Margules parameters and squares represent calculations using a reoptimization of the Berman model with Margules parameters given in chapter 3.

The two models indicate similar trends in Mg cation site occupation as a function of melt composition but our reoptimization predicts significantly less exchange onto the VIII-coordinated site. Regardless of whether the Berman model or the reoptimization is used, this identification of the VIII-fold coordinated Mg population in anorthite is critical for interpreting the Onuma curves as resulting from constant crystal chemical parameters. It would be desirable to obtain high-sensitivity site occupancy data for Mg in anorthite, perhaps by X-ray absorption spectroscopy, to test these model predictions, but such data are not available at this time.

2.3.4 Extension of Lattice Strain Model

The lattice strain model of Blundy and Wood (1994) builds on the strain theory of Brice (1975) to explain the observed near-parabolic dependence (Higuchi and Nagasawa, 1969; Onuma et al., 1968) of logarithmic element partition coefficients on ionic radius. This model ascribes the bulk of isovalent cation partitioning variation to the importance of crystal-site exchange energy, where the strain energy required to fit same-charge cations into a crystal site is a function of the size misfit between the ideal radius of the crystal site and that of the substituting cation and the strain parameter E, the Young's Modulus of the crystal site of interest:

$$\Delta G_{exchange} = 4\pi E N_A \left[\frac{r_o}{2}(r_i - r_o)^2 + \frac{1}{3}(r_i - r_o)^3 \right]. \quad (2.18)$$

The lattice strain model, equation (2.1), collects all potential terms relating to melt component activities, mineral fusion, and activity coefficients of the cation species in

solid and liquid phases into a pre-exponential term, D_o, for a given temperature, pressure, cation charge, and mineral composition.

Graphically, on what have come to be known as Onuma diagrams (logarithm of partition coefficient vs. ionic radius), D_o represents the maximum partition coefficient possible for a site, by a hypothetical cation for which $r_i = r_o$. Fitting Onuma curves through our data (Ca, Ba, Sr, and calculated Mg in VIII-fold coordination using the re-optimized Berman activity model for anorthite field) with the parameters of the lattice strain model show that while no systematic variations in r_o or E exist, as may be expected from the success of the lattice strain model, D_o varies significantly with melt composition. This variation near the top of the parabola is expressed not only in the partition coefficients of the major cation Ca (which are required in this case since stoichiometric anorthite of fixed Ca content is coexisting with a range of liquids of varying Ca content), but also by those of Sr, a trace constituent of similar size.

Figure 2.5(a) shows how well a lattice strain model succeeds in predicting the partitioning behavior of these divalent elements between anorthite and the coexisting melts of this study if D_o is calculated from calcium partitioning data. The crystal chemical parameters for ideal site radius (r_o) and site elasticity (E) are taken from Table 1 of Blundy and Wood (1994) and represent linear extrapolations of the parameters for plagioclases to end-member anorthite. The observed partitioning behavior unexplained by the Blundy and Wood model is represented by an average $\chi^2 = 33$ for each measured D value. We propose that the remaining unmodeled behavior and systematic variation in D_o of our experiments can be quantitatively understood in terms of melt thermodynamics via

a more complex model than that of the ideal quasi-crystalline approach employed in other partitioning studies (e.g., van Westrenen et al., 2001; Wood and Blundy, 1997).

D_o varies not with the stability of anorthite in pure anorthite liquid, as the fusion term was approximated in the original Blundy and Wood (1994) paper, but with the stability of anorthite in an actual liquid of interest, and this is accounted for by its dependence on Al_2O_3 and SiO_2 activity. If one uses a neutral oxide stoichiometric melt model:

$$D_{Ca}^{anorthite/melt} = \frac{1}{X_{melt}^{CaO}} = \gamma_{melt}^{CaO} \, a_{melt}^{Al_2O_3} \, (a_{melt}^{SiO_2})^2 \, e^{[(\Delta G_{fusion}^o + \Delta G_{exchange}^o)/RT]}. \qquad (2.19)$$

This thermodynamic correction to the lattice strain model can be quantified using a self-consistent activity-composition model for non-ideal mixing in the melt phase of interest. We use our reoptimized version of the Berman model for CMAS here; the MELTS model (Ghiorso and Sack, 1995), the MTDATA thermodynamic model (Davies et al., 1990) as used in Blundy et al. (1996), or any other accurate parameterization of silicate liquid activity-composition relations could be used in more complex chemical systems. Equation (2.11) states that D_o actually represents $\gamma_{melt}^{M2+} a_{melt}^{Al2O3} (a_{melt}^{SiO2})^2 e^{\Delta Gofus/RT}$, assuming that γ_{MO} in the solid phase is 1.
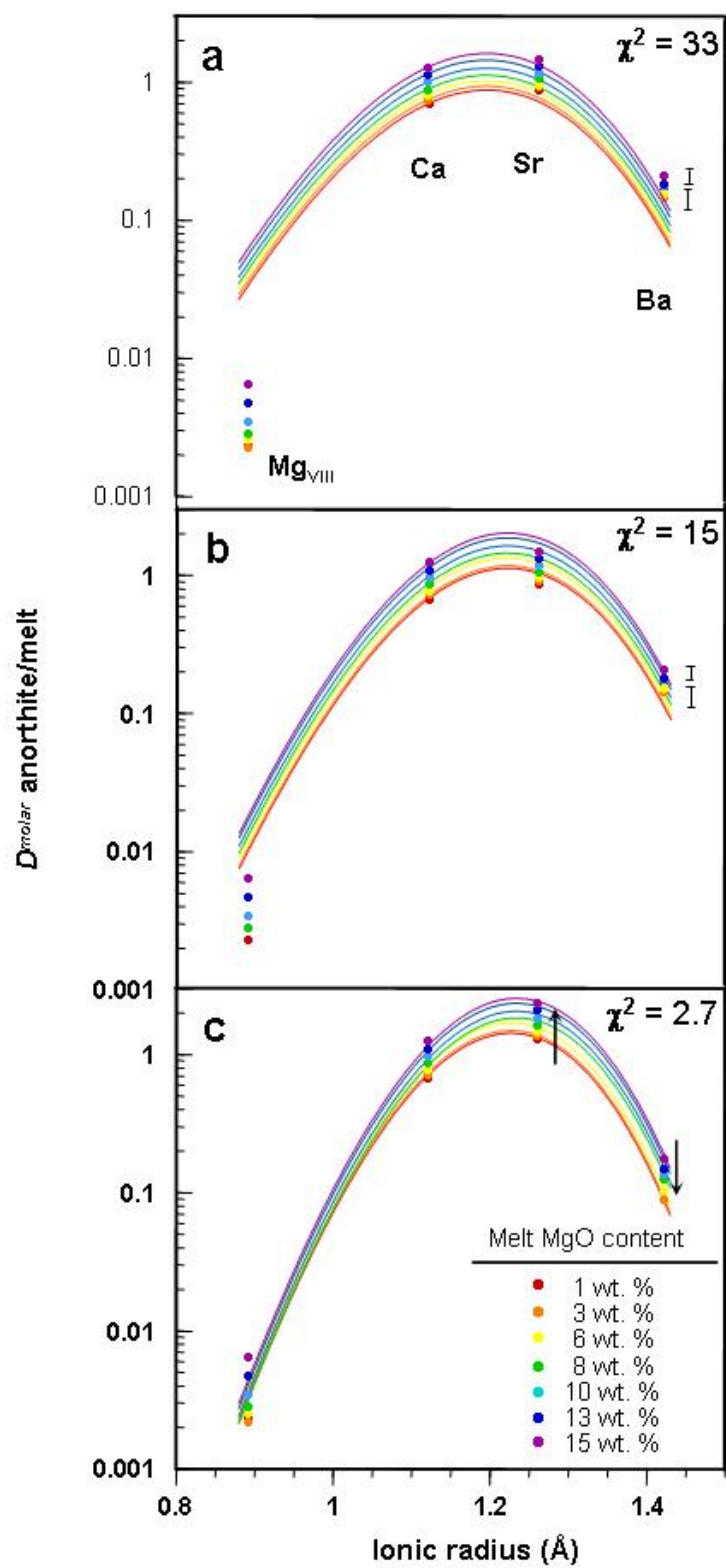
In Figure 2.5(b) we augment the crystal chemical model of partitioning by substituting for D_o the melt activity product $\gamma_{CaO}a_{Al2O3}(a_{SiO2})^2$ for each composition and an unknown common parameter representing $e^{\Delta Gofus/RT}$. Including the crystal chemical parameters E and r_o, this yields a three-parameter solution with an average $\chi^2 = 15$ over the data set of 28 partition coefficients, an improvement on the crystal chemical model.

It should be noted that evidence of deviation from a purely crystal chemical model has been found in comparisons of D values between mineral/silicate and mineral/carbonate liquids (Blundy and Dalton, 2000). The qualitative explanation proposed relates observed variations in E and r_o crystal chemical site fit parameters to energy associated with a structural relaxation in the melt, which adds to the overall solution energy accompanying cation exchange between phases. Van Westrenen et al. (2000) noticed absolute differences in E and r_o that they attributed to the influence of melt composition, but relative variations of these parameters between garnets were dominated by crystal chemistry. If D^{molar}_{Mg} (Table 2.3) were used instead of calculated D^{molar}_{MgVIII} values in our parameterization, the lattice strain parameter E would have to vary substantially (from 97 to 139 GPa) with melt composition to fit the data. Such variation for these melt compositions seems unlikely and requires ignoring evidence of significant Mg tetrahedral site occupancy mentioned in Section 2.3.3. Instead, our treatment of anorthite/silicate partitioning data in this study allows E and r_o to remain constant as crystal chemical parameters with unchanging mineral composition. Deviations from crystal chemistry partitioning theory are interpreted quantitatively via melt component activities within the D_o term.

The remaining difference between our proposed melt major element contribution to the crystal chemical partitioning model and the data is attributed to the influence of the trace cation activities in the melt. The three-parameter partitioning model accounting for melt major element activity shown in Figure 2.5(b) uses melt γ_{CaO} values in place of individual trace element activity coefficients. However, trace element activity coefficients in the melts, while perhaps similar, are unlikely to be identical to γ_{CaO} and a successful partitioning model should account for this. When empirical linear corrections specific to the systematic behavior of D^{molar}_{SrO} and D^{molar}_{BaO} over the differing melt compositions are applied, the γ_{MO}-corrected model produces (with fewer parameters!) an average χ^2 smaller than even that obtained from a free parameterization of D_o, r_o, and E values for each experiment independently (Table 2.4).

Table 2.4 summarizes the performance of several partitioning models:

(1) The Blundy and Wood (1994) crystal lattice strain model contains two parameters, E and r_o, extrapolated to the anorthite endmember from intermediate plagioclase parameterizations. D_o is calculated from D_{Ca} and the resulting average χ^2 equals 33 per datum, where $\chi^2 = [(\ln D^{data}-\ln D^{model})/\ln\sigma^{data}]^2$. The uncertainty associated with calculated D^{molar}_{MgVIII} values remains unknown; for modeling purposes it is assumed to be 0.001.

(2) A free parameterization with D_o, E, and r_o values for each of the seven compositions in this study decreases the χ^2 average considerably to 11, but requires 21 separate parameters to describe our data as there are no systematic variations in r_o or E.

Table 2.4. Comparison of measured data with model parameterization predictions of anorthite/melt partition coefficients. Goodness of fit is defined as χ^2 = average $[(\ln D^{data} - \ln D^{model})/\ln \sigma^{data}]^2$ per datum for Mg_{VIII}, Ca, Sr, and Ba molar partition coefficients and seven melt compositions.

Model	Fit Parameters	χ^2
Anorthite (extrapolated mean), Blundy and Wood (1994) Calculate D_o from D_{Ca}, $r_o = 1.196(18)$ Å, $E = 124.5(14.8)$ GPa	2	33
Mathematica free parameterization: unique D_o, r_o, E solutions for partitioning data of each melt composition	21	11
$D_o \propto \gamma_{melt}^{CaO} a_{melt}^{Al_2O_3} (a_{melt}^{SiO_2})^2 e^{\Delta G_{fus}^o / RT}$ Melt major oxide correction to lattice strain model: D_o is product of major oxide activities and fit parameter (G) representing $e^{\Delta Gofus/RT}$ $G = 4.095 \cdot 10^7$, $r_o = 1.22$ Å, $E = 151.3$ GPa	3	15
$D_o \propto \gamma_{melt}^{cation} a_{melt}^{Al_2O_3} (a_{melt}^{SiO_2})^2 e^{\Delta G_{fus}^o / RT}$ Empirical linear correction for D_{Sr} and D_{Ba} residuals. $G = 5.170 \cdot 10^7$, $r_o = 1.227$ Å, $E = 190.2$ GPa, $\gamma_{melt}^{SrO} \simeq (-0.385 - 0.690 X_{melt}^{MgO}) \gamma_{melt}^{CaO}$ $\quad$ $\gamma_{melt}^{BaO} \simeq (0.568 - 1.933 X_{melt}^{MgO}) \gamma_{melt}^{CaO}$	7	2.7

(3) We can account for melt major oxide activities in D_o by simultaneously solving equation (2.11) for each partition coefficient in all seven melt compositions to minimize a sum of χ^2. In this treatment, the activity coefficients of the cations in anorthite are assumed to be equal to 1 and oxide activity data comes from our reoptimization of the Berman CMAS liquid model. The remaining unknown quantity in equation (2.11) is a value for $e^{\Delta Gofus/RT}$, termed "G," which should remain constant across all seven

compositions. The three-parameter solution for G, E, and r_o generates an average χ^2 of 15.

(4) The residuals of the melt major element activity model (3) are attributed to nonideality of the trace species in the melts. Analytical resolution restricts observable dependence of these residuals on melt composition to linear relationships. However, including slope and intercept parameters for γ_{SrO} and γ_{BaO} relative to known γ_{CaO} as a function of melt X_{MgO} still considerably improves our model. The resulting seven-parameter model yields a $\chi^2 = 2.7$, a better fit with far fewer parameters than the free parameterization of each Onuma curve. Figure 2.5(c) shows the Sr and Ba partitioning data linearly corrected back onto the model Onuma curves as a function of X_{MgO} in the melt.

One should be cautious about using the γ_{MO}-corrected parameterization presented here as an exact, quantitative treatment of the trace cation activity coefficients in these melts. A seven-parameter system to fit these data is degenerate and thus the values of r_o and E influence the extent of correction for partitioning behavior we attribute to the influence of γ_{MO}. Parameters shown in Table 2.4 for this parameterization are a representative, rather than unique, solution. Furthermore, if future magnesium site occupancy data were to demonstrate that the original Berman melt model more accurately predicts magnesium site distributions in anorthite than the reoptimization employed here, the modeled E value for this data would decrease by approximately 20 GPa for both the three- and seven-parameter fits.

We also note a difficult philosophical issue concerning the meaning of the fit parameters r_o and E. Papers by Blundy, Wood and co-workers (Blundy and Dalton, 2000; van Westrenen et al., 2000) have developed models in which these parameters vary with liquid composition and so are not strictly descriptions of the properties of crystals alone. Yet these authors have noted the similarity both between fitted values of r_o and site radii from structure refinements and between fitted vales of E and macroscopic Young's moduli from elastic data, both of the latter data types defining properties of the crystal in isolation. In this work, we remove melt thermodynamics and obtain good fits with values of r_o and E that are independent of melt composition and so could be properties of the isolated crystal, yet the resulting values do not match site radii and mineral elasticity. Neither of these outcomes is entirely satisfactory. It remains an open question whether it is appropriate to think of these parameters in terms of a direct physical interpretation rather than as free parameters of a successful model whose form was originally motivated by physical insight.

2.3.5 Calculating Activity Coefficients of Melt Trace Species

Understanding the precise activity coefficients of trace constituents in silicate liquids is essential to developing complete thermodynamic models of trace element distributions in magmatic systems (e.g., Hirschmann and Ghiorso, 1994). In our experiments, the residual misfit of observed D^{molar}_{Sr} and D^{molar}_{Ba} values to those predicted by the melt composition-modified crystal chemistry model is characterized by a negative slope as a function of melt MgO content. This qualitatively suggests that the activity

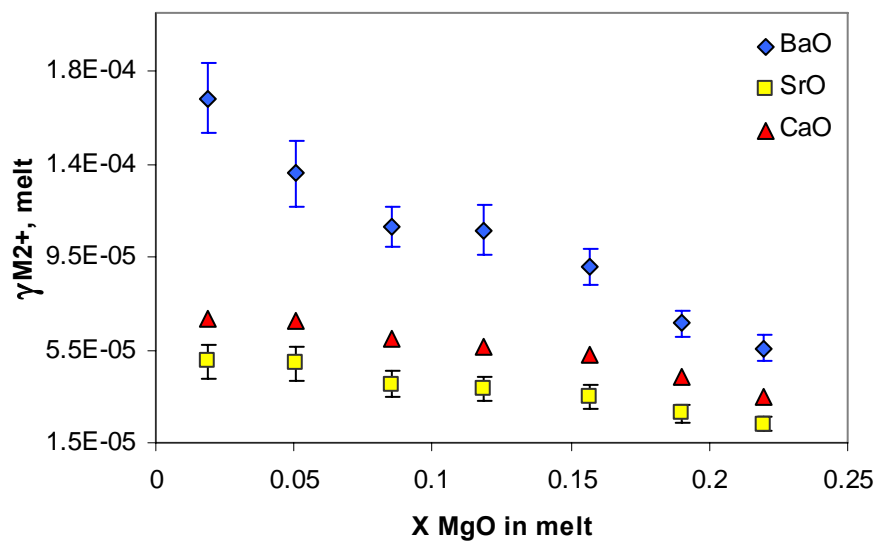coefficients of these neutral trace element species decrease as melts become more magnesian.

Figure 2.6. Calculated melt γ_{BaO} and γ_{SrO} values plotted with γ_{CaO} (from re-optimization of Berman model) for the seven liquid compositions of this study. Error bars are 1σ.

Without independently knowing the activity coefficients of BaO and SrO in the solid phase, γ_{BaO} and γ_{SrO} of the melts cannot be directly solved from equation (2.11). However, Henry's Law for these trace constituents in anorthite is equivalent to a constant value of the activity coefficient in the solid for each oxide, so most of the variation we see is attributable to changes in the melt activity coefficients. We can examine these relative changes by assuming ideal mixing (activity coefficient = 1) of these cations in anorthite. In this case, ΔG^{o}_{fusion} of anorthite can be calculated for each composition from D^{molar}_{CaO} data and then relative values for the melt activity coefficients may be explicitly derived. The compositional trend for both SrO and BaO is similar to that given by the

original or re-optimized Berman models for CaO in our liquids, as shown in Figure 2.6, suggesting a similar network-modifying role in the melt phase.

Exchange equilibria provide additional support for the overall qualitative trends in divalent cation activity coefficients calculated above. The *equilibrium* exchange constant, $K_{D,eq}$, between anorthite and melt for an exchange reaction between Ca^{2+} and Ba^{2+} in coexisting anorthite and melt phases would be,

$$K_{D,\,eq}^{anorthite/melt} = \frac{a_{Ca^{2+}(anorthite)}\,a_{Ba^{2+}(melt)}}{a_{Ca^{2+}(melt)}\,a_{Ba^{2+}(anorthite)}}\,. \tag{2.20}$$

On the other hand, the *observed* exchange partition coefficient $K_{D,obs\ Ca-Ba}^{\quad anorthite/melt}$ is defined as $D^{molar}_{Ca}\,/D^{molar}_{Ba}$. If the activity coefficients of the cations in the anorthite phase remain constant (i.e., Henry's Law behavior) and temperature is constant (making $K_{D,eq}^{anorthite/melt}$ a constant), then the expression for $K_{D,obs\ Ca-Ba}$ may be reduced to,

$$K_{D,obs\ Ca-Ba}^{anorthite/melt} = constant \cdot \frac{\gamma_{Ca^{2+}(melt)}}{\gamma_{Ba^{2+}(melt)}}\,. \tag{2.21}$$

Plots of $K_{D,obs}^{anorthite/melt}$ for Ca-Sr, Ca-Ba, and Sr-Ba exchanges as a function of MgO content in the melt (Figure 2.7) suggest the same trends as the calculated $\gamma_{MO,melt}$ values in Figure 2.6. $K_{D,obs\ Ca-Sr}$ varies little as the network modifying major element content of the melt becomes more magnesian, suggesting that $\gamma_{CaO,melt}$ and $\gamma_{SrO,melt}$ exhibit nearly identical behavior. $K_{D,obs\ Ca-Ba}$ and $K_{D,obs\ Sr-Ba}$ both increase significantly, meaning that γ_{BaO} in the melt systematically decreases relative to γ_{SrO} and γ_{CaO} as X_{MgO} increases. Calculated $\gamma_{MO,melt}$ values (Figure 2.6) from our hybrid melt thermodynamic-crystal chemistry treatment are consistent with this result. More extensive data of this type should allow a general parameterization of these trace activity coefficients in melts, and

hence, in combination with lattice strain theory for crystal chemical effects and major element melt-mineral equilibria for obtaining D_o, will provide the final link in a complete trace element partitioning model.
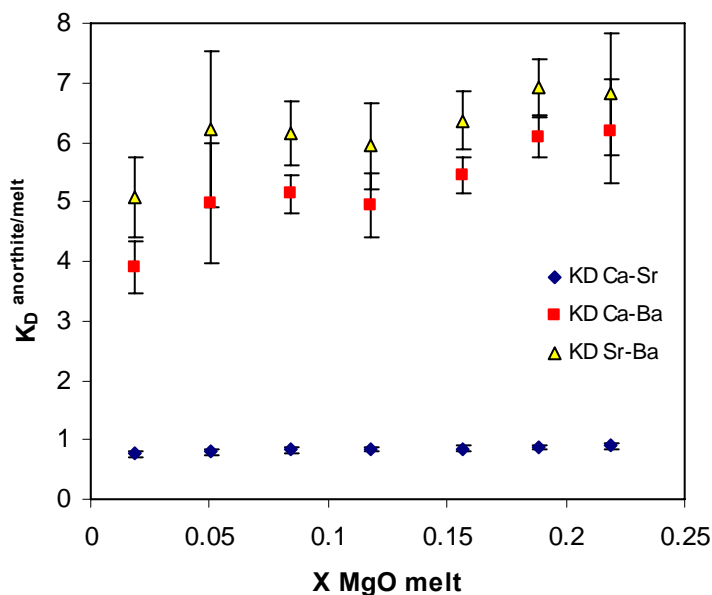

Figure 2.7. Exchange partition coefficients ($K_D = D^{molar}_{M1O}/D^{molar}_{M2O}$) for Ca-Sr, Ca-Ba, and Sr-Ba. Uncertainty is 1σ.

2.3.6 Melt Structure and Partitioning

Quantitative relationships between partitioning and melt properties have yet to be fully elucidated, though studies have attempted to relate partitioning behavior to both melt thermodynamics (Hirschmann and Ghiorso, 1994; Kinzler et al., 1990; O'Neill and Eggins, 2002) and structure (Gaetani, 2004; Kohn and Schofield, 1994; Kushiro and Walter, 1998; Mysen and Dubinsky, 2004). We have approached the problem with an empirical thermodynamic model of the melt, but we also wish to evaluate whether

structural information about the melt provides insight into the origin of the melt activity coefficient variations and their influence on partitioning.

The crystal chemical model of partitioning assumes that the strain imposed on a site within a liquid network by a substituting cation is negligible relative to the strain due to cation misfit on a crystal site. The quality of this assumption may vary with both the structure of the liquid and of the liquidus mineral. Calculation of an average non-ideal mixing chemical potential of BaO from melt γ_{BaO} plotted in Figure 2.6 yields $RT\ln\gamma_{BaO} =$ ~125 kJ/mol at 1330 °C. The $\Delta G^o_{exchange}$ of Ba for the anorthite VIII-site calculated from the crystal chemical portion of our partitioning model is considerably smaller, ~40 kJ/mol, and therefore may have less control over partitioning behavior than would be predicted by a purely crystal chemical model.

Universal melt parameters may offer insights into melt structure as a whole and its effects on trace element partitioning. As shown in Table 2.3, the liquid compositions of this study are essentially isopolymerized in terms of the frequently used parameter NBO/T, representing the ratio of non-bridging oxygens to tetrahedrally coordinated cations in the melt (Mysen et al., 1982). Since NBO/T treats Al^{3+} and Si^{4+} as having identical implications for melt structure and the amounts of both in our melts vary only slightly, NBO/T is not, in this case, a useful parameter for relating our observed partitioning behavior to melt structural changes. However, optical basicity, which estimates the average electron cloud density around oxygen in a liquid (Duffy, 1993; Mills, 1993), varies systematically among our compositions, decreasing as the abundance of more polarizing Mg^{2+} cations increases relative to Ca^{2+}.

We find that the partitioning of all divalent elements considered here onto the anorthite VIII-fold coordination site (Figure 2.8) increases linearly with optical basicity of the melt.
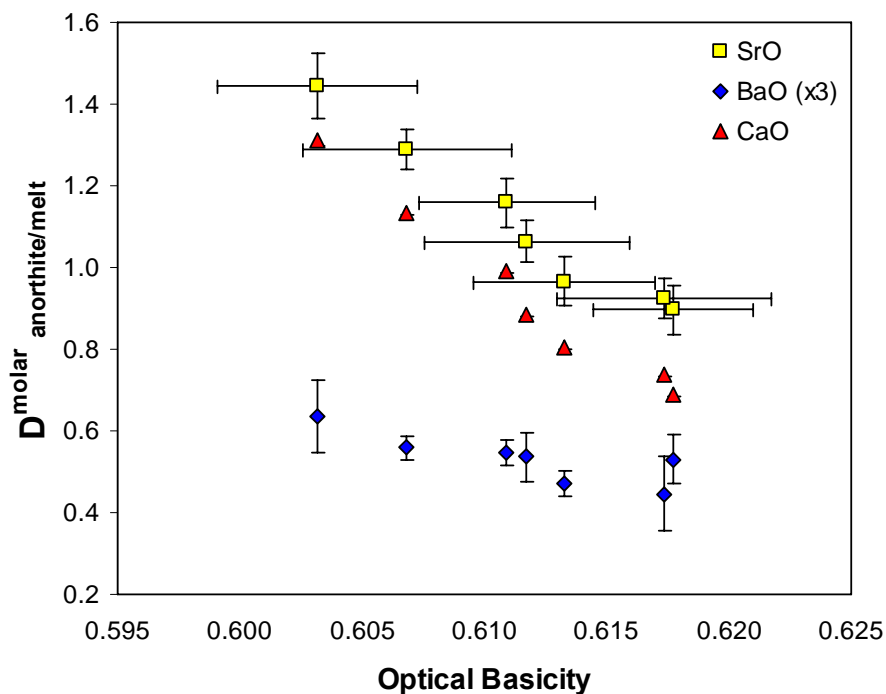

Figure 2.8. D^{molar} as a function of optical basicity (from Mills, 1993). 1σ uncertainty shown in brackets where uncertainty exceeds symbol size except in the case of optical basicity, where error bars have been omitted on CaO and BaO data points for clarity. D^{molar}_{BaO} and associated errors are shown as x3 measured values.

The experimental compositions of this study vary primarily in Mg/Ca (0.05 to 1.2) and to a lesser extent Al/(Al+Si), which is 0.31 in the least magnesian composition and ranges up to 0.35. As melts become progressively magnesian at roughly constant Si and Al contents, more Mg might be forced to charge-balance Al, creating a less stable melt structure relative to that of more calcic compositions.

One consequence may be the formation of a wider range of coordination environments for network modifying cations. This would increase the number of magnesium cations in higher-coordinated melt sites that are energetically competitive with Ca for placement in VIII-fold coordination in anorthite. Studies in both silicate (Fiske and Stebbins, 1994) and aluminosilicate melts (George and Stebbins, 1998) indicate that Mg exhibits lower coordination when in melts composed of lower field strength cations. As the magnesium content of our melts increases, the average Mg coordination number may rise to near 6. Our calculations from melt major oxide thermodynamics predict that Mg increasingly populates the VIII-fold coordinated site of anorthite relative to IV-fold as melt MgO content increases. If the number of coordination sites in a melt were to progressively become more like the population present in a coexisting solid phase, energetic barriers to greater equilibrium substitution into the crystal structure would decrease. By this mechanism, increasingly magnesian melts would promote higher coordination of Mg in anorthite and contribute to changes in D^{molar}_{MgVIII}. Computer simulations of melt solution energies for a cation species suggest that melt coordination environments can significantly influence predicted partition coefficients (van Westrenen et al., 2000).

Another approach to characterizing melt structure considers the number of oxygen bonds available to network modifying cations. Local polymerization in silicate liquids is often described in terms of Q^n species, where n represents the number of bridging oxygens to which a tetrahedrally coordinated cation such as Si or Al is bound in the melt framework (Stebbins, 1995). Fully polymerized tetrahedral networks contain only Q^4 species in which each oxygen (BO) is bonded between two tetrahedral units, while fully

depolymerized networks are composed of Q^0, or non-bridging oxygens (NBO). Spectroscopic investigation of the liquid structures in the CMAS system has been hampered by poor peak resolution, particularly at high temperature. However, study of alkali aluminosilicate melts (Mysen, 1997; Mysen, 1999) may yield qualitative insights into liquid structures in alkaline earth systems. In alkali aluminosilicates for this Al/(Al+Si) range at 1400 °C, approximately 70 % of the bonding environments are Q^4, with perhaps 20 % as Q^3 and Q^2; less than 10 % of oxygens are Q^1 [Mysen, 1997]. A slight trend towards formation of Q^4 and Q^2 at the expense of Q^3 units, creating a more disordered melt structure, may occur over our compositional range as Al/(Al+Si) increases according to the reaction,

$$2\,Q^3 = Q^2 + Q^4. \tag{2.22}$$

However, any influence the minor Al/(Al+Si) change may exert on melt structure cannot be separated here from the potentially large influence of the major network modifying cations present, since greater magnesium content also has been implicated in increasing the number of Q^4 and Q^2 units in a melt. Hence our data are not necessarily inconsistent with the prediction of Mysen (2004) that network modifying trace element mineral-melt partition coefficients should show a negative correlation with melt Al/(Al+Si). Mysen and Dubinsky (2004) state that abundances of Q^n species are not only a function of melt polymerization, but also a function of ionization potential of the network modifying cations, which form energetically non-equivalent bonds with NBO according to their relative abilities to draw electrons from oxygen. Cations with smaller ionic radii and/or greater charge will form less stable bonds with NBO (mostly Q^3 species in these melts), and this stabilizes larger populations of Q^2 and Q^4 species according to

equation (2.22). This effect has been documented by Libourel et al. (1992), who observed increases in ^{29}Si peak shielding with magnesium content in CMAS glasses. They interpreted this as a possible consequence of a greater variety of Si sites available in the glass structure, which would translate into a greater range of Q^n speciation, as would occur when forming Q^2 and Q^4 species from Q^3. Merzbacher et al. (1990) also noted that ^{29}Si peaks in MAS glasses were broader than those of CAS.

A wider distribution of oxygen species due to destabilization in melts of higher magnesium content may result in a greater abundance of coordination sites energetically comparable to those within the anorthite structure, which is composed of a purely Q^4 framework encasing larger VII-fold coordinated sites occupied by a divalent network modifying cation to charge balance Al^{3+}. In this scenario, all alkaline earth cations occupying such melt sites would partition more strongly into the anorthite structure as melts become more magnesian, as observed in this study.

2.4 CONCLUSIONS

We demonstrate that melt composition affects trace element partitioning behavior in a manner that can be systematically accounted for by projecting melt model refinements onto existing crystal lattice strain models of partitioning (Beattie, 1994; Blundy and Wood, 1994). Here our model relies on an empirical description of melt thermodynamics, but this approach to partition coefficient determination may be applied using any self-consistent thermodynamic melt model, such as MELTS in the case of natural compositions, providing that the mineral thermodynamics are well characterized.

Such a treatment shows promise in generating more accurate predictions of D values that would be costly or, in the case of short-lived radioactive elements, potentially hazardous to obtain experimentally. Our method also offers a means for isolating activity coefficient behavior of melt trace species. Such information has been hitherto inaccessible yet, as our study demonstrates, may often play a non-trivial role that should be incorporated into a complete model of trace element partitioning.